J|A|C|S
ARTICLES
Published on Web 03/11/2006

Hyperbaric Laser Chemical Vapor Deposition of Carbon Fibers from the 1-Alkenes, 1-Alkynes, and Benzene

James L. Maxwell,*,† Mats Boman,‡ Robert W. Springer,† Jaikumar Narayan,§ and Saiprasanna Gnanavelu§

Contribution from the International, Space, and Response Division (ISR-5), Los Alamos National Laboratory, Los Alamos, New Mexico, Inorganic Chemistry Department, Uppsala University, Uppsala, Sweden, and Institute for Micromanufacturing, Louisiana Tech University, Ruston, Louisiana

Received November 18, 2005; E-mail: jmaxwell@lanl.gov

Abstract: The growth of long carbon fibers was investigated using hyperbaric-pressure laser chemical vapor deposition (HP-LCVD). Precursors included the unbranched alkenes with linear structure 1-C_xH_{2x} (where $x = 2,4,5,6,7,8$), the unbranched alkynes, i.e., 1-C_xH_{2x-2} (where $x = 3,4,5,6,8$), and benzene. Rate constants, reaction orders, and apparent activation energies were derived for each precursor over a range of experimental conditions. Axial growth rates from the alkenes were 1−2 orders of magnitude greater than for the alkynes, while growth rates for benzene exceeded 10 mm s^{-1}. Generalized expressions for the growth rate vs molecular weight were determined. For the alkenes, the growth rate was directly proportional to the square root of the precursor molecular weight, while the alkynes exhibited an inverse relationship. Two regions of differing reaction order were identified for the alkynes; at pressures less than 2.0−2.5 bar, the average reaction order was 3.07, while above 2.0−2.5 bar, reaction orders diverged. Expressions were derived for the fraction of carbon atoms deposited per alkyne molecule transported; the deposition efficiency decreased with molecular weight for the alkynes, due in part to the Soret effect. In contrast, the reaction order for the alkenes was 1.65, and for benzene was 2.25. A phase change in the deposit was observed for both the alkenes and alkynes, with the exceptions of pentene and pentyne. Complete axial rate equations for the alkenes and alkynes were derived, as well as volumetric growth equations for the alkynes. It was shown that the volumetric rate increases nonlinearly with laser power at sufficiently high pressures.

I. Introduction

High-purity carbon fibers are important in applications ranging from field-emitter arrays[1] to reinforced composites.[2] Unlike traditional approaches to C-fiber production, such as PAN and pitch pyrolysis,[3,4] hyperbaric-pressure laser chemical vapor deposition (HP-LCVD) is a containerless process,[5] allowing modulation of fiber morphology while eliminating impurities and surface defects which limit fiber strength. Several authors have studied carbon fiber growth with HP-LCVD, using precursors such as ethene,[5,6] methane,[7] and acetylene.[8]

During HP-LCVD, fibers are grown by focusing a laser beam onto a substrate, as illustrated in Figure 1. A gaseous precursor is introduced into the reaction vessel at hyperbaric pressures, and the precursor decomposes at the laser-heated zone to produce a solid carbon deposit. If the laser focus tracks backward, long fibers can be grown, as shown in Figure 2. More complex structures can also be created, such as helical coils, by continuously reorienting and scanning the laser beam.[9]

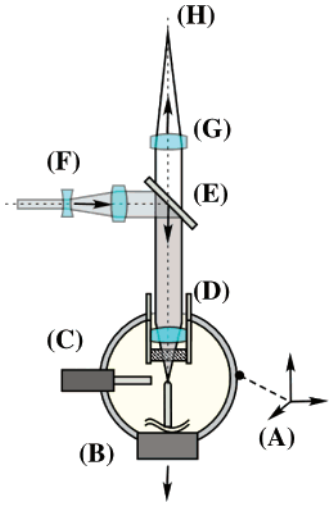

Figure 1. Components of the HP-LCVD apparatus.

† Los Alamos National Laboratory.
‡ Uppsala University.
§ Louisiana Tech University.

(1) Sheshin, E. P. *Appl. Surf. Sci.* **2003**, *215*, 191−200.
(2) Gadow, R.; Kern, F.; Ulutas, H. *J. Eur. Ceram. Soc.* **2005**, *25*, 221−225.
(3) Manocha, L. M.; Bhatt, H.; Manocha, S. M. *Carbon* **1996**, *34*, 841−849.
(4) Xie, J.; Wang, X.; Deng, J.; Zhang, L. *Appl. Surf. Sci.* **2005**, *250* (1−4), 152−160.
(5) Dean, R. N.; Nordine, P. C.; Chrstodoulou, C. G. *Microwave Opt. Technol. Lett.* **2000**, *24* (2), 106−111.
(6) Kargl, P. B.; Arnold, N.; Bauerle, D. *Appl. Surf. Sci.* **1997**, *108*, 257−262.
(7) Fauteux, C.; Longtin, R.; Pegna, J.; Boman, M. *J. Appl. Phys.* **2004**, *95* (5), 2737−2743.
(8) Lackey, W. J.; Jean, D.; Duty, C.; Johnson, R.; Bondi, S. *Carbon* **2002**, *40* (9), 1435−1445.

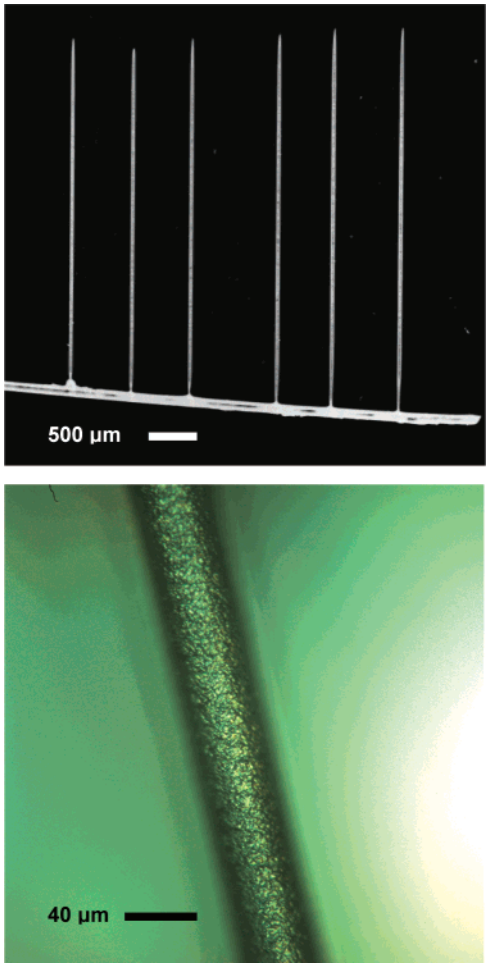

Figure 2. Carbon fibers, (A) typical fiber array, (B) Nomarsky micrograph of C-fiber grown from ethene at 3.3 bar.

In this work, three classes of hydrocarbon precursors were investigated for the deposition of *carbon* fibers and related microstructures: the 1-alkenes (i.e., C_xH_{2x}), the 1-alkynes (i.e., C_xH_{2x-2}), and the basic aromatic hydrocarbon, benzene (C_6H_6). Fibers were grown from aliphatic chains of two to eight carbon atoms, with the exception of propene and heptyne which were not included in this study. For simplicity, the location of double and triple bonds in the aliphatic compounds was restricted to the end of each chain. Branched hydrocarbons, *n*-isomers of $n > 1$, the alkanes, and more complex aromatic compounds are deferred to future work. Comparisons are made between hydrocarbons of similar structure but of varying molecular weights and hybridization—identifying differences in transport that control growth rates during HP-LCVD.

II. Experimental Details

The experimental apparatus employed for the fiber growth experiments is shown in Figure 1. A chamber with a 2-in. internal diameter was mounted on a moveable stage (A), so that the chamber could be aligned to the focused laser beam. In addition, a precision retractable sample holder (B) was used for tracking the growth front. During all growth experiments, the region of *steady-state* growth was identified using a method described previously.[9,10] An adjustable nozzle (C), for introducing gases into the chamber, was oriented toward the laser focus. The laser beam was focused onto the substrate through a 60-mm focal length best-form lens and recessed sapphire window mounted on the chamber (D); the window and chamber were heated to prevent gas condensation which could potentially alter the precursor pressure. The $1/e^2$ laser beam waist was approximately 14 μm in diameter as measured by a rotating knife-edge. Both Ar^+ (at 488/514 nm) and Nd:YAG (at 532 nm) cw lasers were employed, and the laser beams were introduced through the long-pass beam splitter (E) and beam expander (F). A near-IR achromat (G) was employed to re-image the reaction zone at point (H). This made it possible to perform real-time measurements of the fiber tip temperature during all stages of the growth, using a pinhole placed at (H) with subsequent infrared filters and detectors. Temperatures were calibrated using a blackbody source. Growth rate measurements were obtained by monitoring the growth with calibrated video microscopes (not shown).

III. Theory

Deposition kinetics can be modeled using the equation:

$$\ln(k) = \ln(k_o) + n\ln(\mathrm{P}) - \frac{E_a}{RT} \tag{1}$$

Here, k is the reaction rate, k_o is the rate constant, n is the reaction order, P is the precursor pressure, E_a is the activation energy, R is the universal gas constant, and T is the temperature. For data involving multiple precursors of similar structure, a more generalized expression is applied that assumes a functional form, *f(m)*, for molecular weight dependencies:

$$\ln(k) = \ln(k_o) + \ln[f(m)] + n\ln(\mathrm{P}) - \frac{E_a}{RT} \tag{2}$$

f(m) can be measured from growth rate data where the pressure and temperature are held constant while varying the precursor molecular weight.

A functional form for *f(m)* can also be estimated from first principles. For diffusion-limited reactions, the overall transport of carbon depends on the rate of mass flux across the boundary layer, $\vec{J}_1$, the fraction of precursor molecules reacting at the surface, χ_r, and the fraction of mass deposited per reacting precursor molecule, χ_m. From continuity, the mass growth rate, $\dot{m}_d$, per unit area, A, is:

$$\frac{\dot{m}_d}{A} = \chi_r\chi_m\vec{J}_1\cdot\hat{n} \tag{3}$$

Assuming mass-transport-limited conditions, the axial growth rate, k_n, at the fiber tip is therefore proportional to:

$$k_n \propto \frac{\chi_m}{\pi r_s^2\rho_d}\vec{J}_1\cdot\hat{n} \tag{4A}$$

where ρ_d and r_s are the deposit density and the steady-state fiber diameter, respectively.

During diffusion-limited HP-LCVD, concentration gradients and strong temperature gradients drive the transport. Let $m_{p,1}$ and $m_{p,2}$ be the molecular masses of the precursor and byproducts, respectively, $\bar{m}_p$ the mean molecular mass of the gas mixture, α_t be the thermal diffusion ratio, and D_{12} the mass diffusivity. Then, for binary gas mixtures where the

(9) Williams, K.; Maxwell, J.; Larsson, K.; Boman, M. *Proceedings of the IEEE Micro Electro Mechanical Systems (MEMS)* **1999**, 232−237.

(10) Maxwell, J.; Boman, M.; Springer, R. W.; Nobile, A.; Defriend, K.; Espada, L.; Sandstrom, M.; Kommireddy, D.; Pegna, J.; Goodin, D. *Adv. Funct. Mater.* **2005**, *15*, 1077−1087.

concentration of one species is small relative to another, eq 4A becomes:[11]

$$k_n \propto \frac{\chi_m}{\pi r_s^2 \rho_d} \rho_g D_{12} \left[\nabla n_1 + \frac{m_{p,1} \cdot m_{p,2}}{\bar{m}_p^2} \alpha_t \nabla \ln(T) \right] \cdot \hat{n} \quad (4B)$$

Observe that extreme temperature gradients in excess of 10^6-10^7K/m can be present in the gas near the fiber tip—even for moderate laser powers (e.g., 0.5−2.0 W). As a result, it is possible for thermodiffusion (the Soret effect) to dominate transport during HP-LCVD—as has been observed in localized transport within flames.[12]

Now, for the alkynes, it will be shown that the generation of byproduct gas species is small relative to the concentration of the primary gas species. However, when α_t in eq 4B is negative, the concentration of reaction byproducts near the deposit surface may be enhanced due to the Soret effect.[13,14] For molecular hydrogen diffusing through the alkynes, values of $(m_{p,1} \cdot m_{p,2}/\bar{m}_p^2) \cdot \alpha_t$ range from −0.075 (butyne) to −0.027 (octyne). The reaction rate is suppressed as alkyne molecules are displaced by hydrogen near the fiber surface. This effect is even more prominent as $m_{p,1} \gg m_{p,2}$, i.e., where the byproduct molecular weight is small relative to the precursor.

In eq 4B, the deposition rate is also influenced by the molecular weight dependence of the diffusivity, D_{12}. Defining σ_{12} as the mean collisional cross-section, $\sigma_{12} = {}^1/_2(\sigma_1 + \sigma_2)$, Ω^* as the self-diffusion integral, and N_a as Avogadro's number, then assuming rigid elastic spheres, a well-known expression for D_{12} is:[15,16]

$$D_{12} = \frac{3}{8\sigma_{12}^2 \Omega^* P} \sqrt{\frac{R^3 T^3 (m_{p,1} + m_{p,2})}{2\pi N_a^3 (m_{p,1} \cdot m_{p,2})}} \quad (5)$$

At high temperatures, Ω^* approaches a constant,[16] and is nearly independent of molecular weight. The collisional cross-section is also a weak function of $m_{p,1}$ and $m_{p,2}$ which can be determined from van der Waals equation and empirical viscosity data. Therefore, assuming $m_{p,1} \gg m_{p,2,}$ and $\sigma_1 \gg \sigma_2$, and defining $\chi = 1,2,...$ as the number of carbon atoms in each chain, the dependence of the growth rate on molecular weight can be approximated by:

$$k_n(m_p) \tilde{\propto} \frac{\chi_m m_p^{+1/2}}{\sigma_1^2} \tilde{\propto} \chi_m \cdot \chi^{+1/2} \quad (6)$$

This holds for comparisons between two like precursors under identical pressures and temperature gradients. From eq 6, we can see that, if all carbon atoms per reacting molecule are deposited at the surface (i.e., $\chi_m \rightarrow 1$), the reaction rate increases as longer hydrocarbon chains are employed. Generalizing eq 6 for *f(m)* in eq 2, one obtains the functional form:

$$f(m) \equiv k_m \cdot m_p^{\xi} \quad (7)$$

IV. Results

Dozens of fibers were grown from the alkynes, alkenes, and benzene—and their steady-state diameters, peak tip temperatures, and axial growth rates were measured. All fibers were grown under diffusion-limited conditions; i.e. their axial growth rates could not be increased significantly by supplying additional laser power. Previous studies have shown the axial mass-transport limit (a-MTL) for ethene to occur at laser powers of approximately 350−450 mW for pressures between 1 and 8.0 bar;[10] it was also shown that fiber diameters saturated above laser powers of 400−600 mW (see Figures 2−3, 6 of ref 10). As ethene possesses the least molecular weight and greatest self-diffusivity of all the precursors in this study, it follows that all fibers were at (or within) the a-MTL condition (≥350−450 mW). Temperatures were measured using the pinhole technique described earlier and tracked closely Figure 4 of ref 10; temperatures also follow calculations from eqs 3A−4D of the same reference.

Molecular Weight. Reaction rates, pathways, and the surface adsorption were found to differ greatly with precursor structure. Comparing axial growth rate data in Figure 3, several trends are immediately apparent. First, especially at low pressures, growth rates differ by over 1 order of magnitude between the two aliphatic groups—the alkenes grow at 10^2-10^3 μm s^{-1}, while the alkynes grow at 10^1-10^2 μm s^{-1}. Second, there is an inverse relationship between the growth rate and precursor molecular weight for the alkenes and alkynes; the alkenes grow more rapidly with increasing molecular weight, while the alkynes grow more rapidly with decreasing chain lengths. Third, the relative spread in growth rates within each group is greatest for the alkynes; this spread increases with pressure for the alkynes, while it decreases for the alkenes. Clearly, there is a difference in the mechanisms of reaction and transport for these two classes of carbon precursors—and these differences are related to each precursor's functional group and molecular weight.

For the alkene series, a two-variable regression fit to eq 7 at constant temperature is shown in Figure 4A. The molecular weight exponent, ξ, was found to be 0.57 ± 0.07. This is consistent with diffusion-limited growth rates—where nearly all carbon atoms are deposited per reacting molecule ($\chi_m \approx 1$).

In contrast, data for the alkynes follows an *inverse* relationship with molecular weight, i.e.:

$$k_n \propto m_p^{\xi} \quad (8)$$

where $\xi < 0$. Such inverse relationships can be induced by the Soret effect, where the reaction byproducts are small relative to the precursor(s). However, it is also possible that not all carbon atoms within the alkyne chains are transported to (or remain at) the fiber surface. In Figures 3 and 4B, two distinct growth regimes are apparent, labeled regions (A) and (B). Region A occurs at pressures below 2.0−2.5 bar; in this case, a regression fit gives $\xi = -1.67 \pm 0.07$. Within region B, the spread of growth rates is more extreme, and $\xi = -3.42 \pm 0.15$. Note that the value of ξ in region B is twice that of region A, within the standard error.

(11) Kays, W. M. *Convective Heat and Mass Transfer*; McGraw-Hill: New York, 1966; pp 15−16.
(12) Palle, S.; Nolan, C.; Miller, R. S. *Phys. Fluids* **2005**, *17*, 103601, 1−19.
(13) Garcia-Ybarra, P. L.; Castillo, J. L. *J. Fluid Mech.* **1997**, *336*, 379−409.
(14) Bauerle, D. *Laser Processing and Chemistry*, 2nd ed.; Springer-Verlag: New York, 1996; pp 313−314.
(15) Chapman, S.; Cowling, T. G. *The Mathematical Theory of Non-Uniform Gases*; Cambridge University Press: New York, 1961; p 245.
(16) Fan, J. *Phys. Fluids* **2002**, *14* (12), 4399−4405.

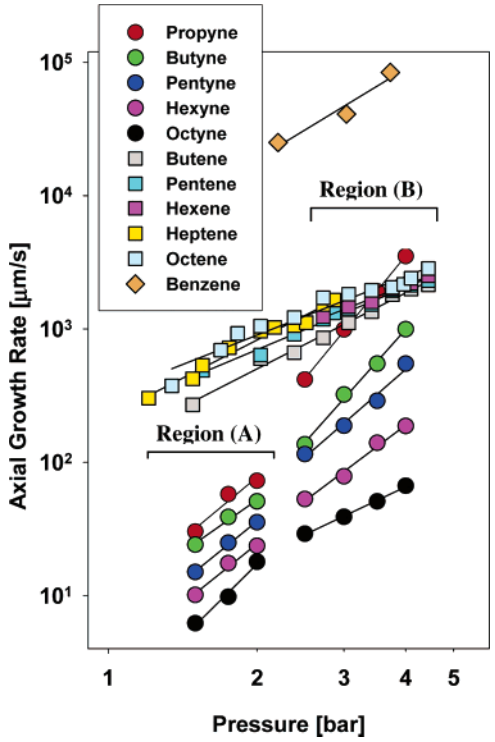

Figure 3. Axial growth rate vs. precursor pressure for the alkenes (950 mW), alkynes (850 mW), and benzene (950 mW).

From eqs 6 and 8, the linear regression results from A and B of Figure 4, and the chemical formula for the alkynes, it is possible to estimate the dimensionless fraction of carbon atoms per reacting alkyne molecule that are permanently incorporated into the fiber surface, χ_d. First, we define the mass per molecule, m_P, as:

$$m_p = 12\chi u + (2\chi - 2)u \tag{9}$$

where u is the atomic mass unit. Then, the mass deposited per molecule, m_d, is:

$$m_d = \chi_m m_p \equiv 12\chi_d \chi u \tag{10}$$

Solving eq 10 for χ_m, substituting m_p from eq 9 into eq 10, and then replacing both χ_m and m_p into the left-hand side of eq 6, we arrive at the relation:

$$k \propto 12\chi_d \chi \sqrt{\frac{u}{14\chi - 2}} \tag{11}$$

In addition to this derived relation, the growth rate is proportional to the empirical results from eq 8. So, for region A:

$$k \propto {m_p}^{-1.67\pm0.07} \approx {m_p}^{-5/3} \tag{12A}$$

and for region B:

$$k \propto {m_p}^{-3.42\pm0.15} \approx {m_p}^{-10/3} \tag{12B}$$

Equating eqs 12A and 12B with eq 11, and solving for χ_d in each case, one arrives at expressions for the fraction of carbon atoms/molecule that are deposited, i.e.

$$\chi_{d,A} \propto \frac{1}{12\chi u(14\chi u - 2u)^{7/6}} \tag{13A}$$

and

$$\chi_{d,B} \propto \frac{1}{12\chi u(14\chi u - 2u)^{17/6}} \tag{13B}$$

Normalizing to the case of $\chi = 1$, one finds the absolute fractions:

$$\chi_{d,A} \approx \frac{1}{\chi}\left[\frac{6}{7\chi - 1}\right]^{+7/6} \tag{14A}$$

and

$$\chi_{d,A} \approx \frac{1}{\chi}\left[\frac{6}{7\chi - 1}\right]^{+17/6} \tag{14B}$$

Note that the exponent in eq14A is approximately equal to 1, while that for eq 14B is approximately 3. However, the difference between the actual value of the exponents and these approximate values is greater than the standard error, defined as the ratio of the standard deviation to the square root of the number of samples. Thus, the difference is statistically significant.

Numerical values of χ_d for the lower-order alkynes up to $\chi = 8$ are given in Table 1. It is important to point out that absolute comparisons between regions A and B are not possible—as their respective columns are not normalized to the same basis. So, it is not possible to state that the process is less efficient for 1-propyne in region B versus region A. However, comparisons within each column *are* possible. Observe that the longer the alkyne chain, χ, the smaller the fraction of carbon atoms incorporated, χ_d. In contrast, the alkenes show little dependence of χ_d on χ.

Reaction Orders. An interesting feature of Figure 3 is that, with increasing pressure, data in the *alkenes* series converge toward a common growth rate, while the *alkynes* data diverges. Table 2 provides reaction orders and rate constants for the alkenes, based on linear regression fits to the data in Figures 3 and 4A. The natural log of the rate constant averages 5.44 (i.e., 231 μm s^{-1}), while the average reaction order is approximately 1.65 between $\chi = 4$ and $\chi = 8$. Note that the rate constant increases slightly with molecular weight, while the reaction order is similar for all of the alkenes.

In contrast, the alkynes show two regions (A) and (B) of differing reaction order. From Figures 3 and 4B, the transition between these regions lies at approximately 2.0−2.5 bar. Table 3 gives derived reaction orders and rate constants for the data in Figure 4B using linear regression fits within each region. For region (A) all of the alkynes follow a similar average reaction order, $n \approx 3.07$, nearly twice that of the alkene average. In region (B), however, individual alkyne curves diverge from the average; n increases for the lower-order alkynes and decreases for the higher-order alkynes. While the *average* reaction order increases slightly to 3.29 within region (B), the reaction order for 1-propyne *increases* to 4.51, while that for 1-octyne *decreases* to 1.75.

Cyclic Hydrocarbons: Benzene. For comparison, fibers were also grown from the cyclic hydrocarbon, benzene (C_6H_6)—refer to the upper-most curve of Figure 3. For any given pressure, the growth rate was more than 1 order of magnitude greater than the alkenes, and 2−3 orders of magnitude greater than the alkynes. Fitting the benzene curve to eq 1, the natural log of the rate constant was found to be 8.29 (i.e., 3980. μm s^{-1}), while the reaction order was 2.25.

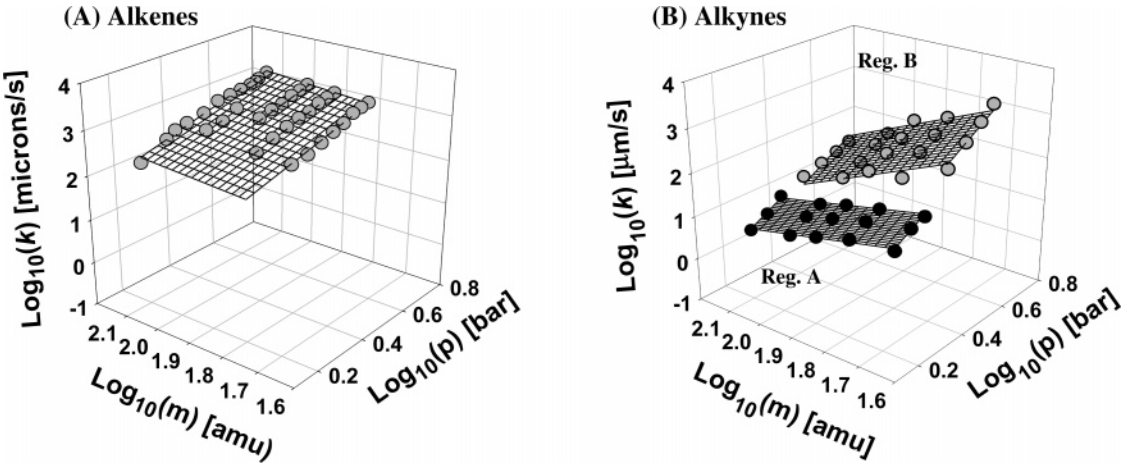

Figure 4. Linear regression fits to growth rate vs. molecular weight and pressure; (A) alkenes, where $\ln(k) = 5.44 + 0.57\ \ln[m_p] + 1.65\ \ln(P) - E'_a/RT$; (B) alkynes, where in region A, $\ln(k) = 1.46 - 1.67\ \ln[m_p] + 3.07\ \ln(P) - E'_a/RT$, and in region B, $\ln(k) = 1.58 - 3.42\ \ln[m_p] + 3.29\ \ln(P) - E'_a/RT$.

Table 1. χ_d Values for the 1-Alkynes vs Chain Length, χ

χ	$\chi_{d,A}$	$1/\chi_{d,A}$	$\chi_{d,B}$	$1/\chi_{d,B}$
3	0.082	12.2	0.011	90.9
4	0.043	23.3	0.0035	286.
5	0.026	38.5	0.0015	667.
6	0.018	55.6	0.00072	1390.
7	0.013	76.9	0.00039	2560.
8	0.0094	106.	0.00023	4350.

Table 2. Rate Constants, k_o and Reaction Orders, n, for the Alkenes

precursor	$\ln(k_o)$	n
1-propene	–	–
1-butene	4.90	1.89
1-pentene	5.48	1.55
1-hexene	5.64	1.45
1-heptene	5.41	1.9
1-octene	5.78	1.46
av	5.44	1.65

Table 3. Rate Constants, k_o, and Reaction Orders, n, for the Alkynes

precursor	$\ln(k_o)$ reg. A	n(A)	$\ln(k_o)$ reg. B	n(B)	ratio B/A
1-propyne	2.21	3.08	1.91	4.51	1.46
1-butyne	2.14	2.61	1.13	4.16	1.59
1-pentyne	1.50	3.00	1.73	3.23	1.08
1-hexyne	1.13	2.97	1.38	2.79	0.94
1-heptyne		–	–	–	–
1-octyne	0.30	3.67	1.75	1.75	0.48
av	1.46	3.07	1.58	3.29	1.11

Three factors ultimately contribute to benzene's extreme growth rates. First, benzene is known to adsorb readily on graphite—with the aromatic ring lying parallel to the graphite surface;[17] as a result, all six carbon atoms have a high probability of being incorporated into the deposit—making the overall carbon transport highly efficient. Second, the benzene ring is already in the form of a graphene sheet, and the π-orbitals of the precursor and deposit are highly symmetric. Evoking Woodward–Hoffmann rules for the conservation of orbital symmetry,[18] deposition kinetics should occur more rapidly for benzene than for aliphatic hydrocarbons of lesser symmetry. Adding to this, it was observed that fibers grown from benzene were more graphitic in cross-section than their aliphatic counterparts, supporting previous reports that highly oriented graphite is obtained during the CVD of benzene.[19] Finally, the benzene molecule has the highest *ratio* of carbon mass to molecular mass (C_xH_x) of all the precursors in question, so that under identical pressures it will transport carbon more rapidly than any aliphatic molecule of identical χ-value.

Activation Energies. Axial fiber growth rates over a wide range of laser-induced temperatures are given in Figure 5, A and B, for the alkenes and alkynes, respectively. The pressure of each precursor was held constant at 2.0 bar for all fibers in Figure 5, A and B, while every fiber was grown at a steady laser power corresponding to a specific temperature. *Steady state* average and peak tip temperatures were obtained using methods described previously.[10]

As all the fibers in this study were grown within the mass-transport-limited (MTL) regime, only *apparent* activation energies (E'_a), can be obtained from our data. Within Figure 5A, for example, the right-most data points, where $(1/T_{av})1000 \approx 0.72-0.74$, lie on the boundary between the kinetically limited and MTL regimes (at laser powers of ~330–350 mW); all points to the left are well within the MTL regime. In Figure 5B, laser powers begin at 450–470 mW—above the mass transport limit.

While activation energies, such as in eqs 1–2, provide kinetic information, *apparent* activation energies (E'_a) provide information on the rate-limiting step in the transport of each precursor—and can be used to identify changes in transport mechanism(s). Alternatively, where transport mechanisms remain unchanged, E'_a can provide information on structural changes in the deposit vs temperature, such as packing density differences from changes in phase.

An important feature of both A and B of Figure 5 is the change in slope at $1/T_{av}(1000) \approx 0.45-0.50$; this transition is apparent for most alkene and alkyne precursors—with the potential exception of pentene and pentyne—and the transition is bracketed with vertical lines in Figure 5, A and B. For octene, additional data is unavailable to definitively observe this transition.

(17) Bardi, U.; Magnanelli, S.; Rovida, G. *Langmuir* **1987**, *3* (2), 159–163.
(18) Woodward, R. B.; Hoffmann, R. *The Conservation of Orbital Symmetry*; Academic Press Inc.: New York, 1971; p 37.
(19) Yoshimoto, Y.; Suzuki, T.; Hagashigaki, Y.; Nakajima, S. *Thin Solid Films* **1988**, *162*, 273–278.

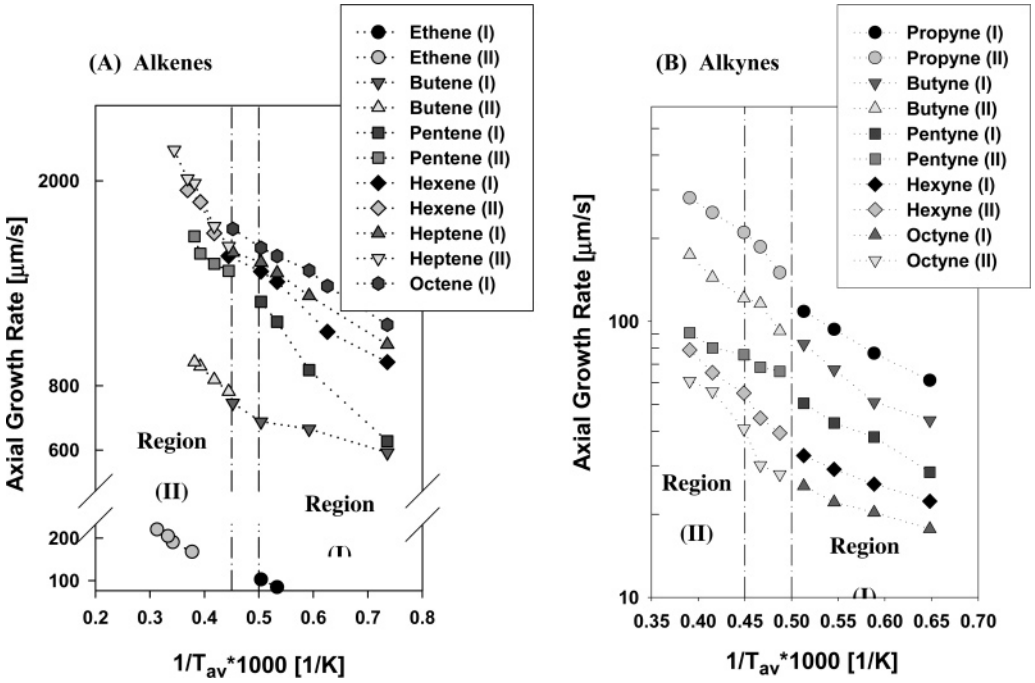

Figure 5. Axial growth rates vs. inverse laser power, (A) alkenes, (b) Alkynes in regions (I) and (II). pressure held constant at 2.0 bar in All cases.

Table 4. E'_a of Alkenes at $P_o = 2.0$ bar: Transport-Limited Apparent Activation Energies, E'_a, [kJ/mol], and Rate Constants [μM s^{-1}] for Zones (I) and (II)

	region I		region II	
precursor	ln(k_o)	E'_a	ln(k_o)	E'_a
ethene	6.76	70.34	7.21	94.37
1-butene	6.92	12.03	7.61	35.69
1-pentene	8.39	44.45	8.18	37.08
1-hexene	8.05	28.80	9.03	65.49
1-heptene	7.98	24.95	9.23	72.04
1-octene	8.06	24.72	8.92	56.42

Table 5. E'_a of Alkynes at $P_o = 2.0$ bar: Transport-Limited Apparent Activation Energies, E'_a, [kJ/mol], and Rate Constants [μM s^{-1}] for Regions (I) and (II)

	region I		region II	
precursor	ln(k_o)	E'_a	ln(k_o)	E'_a
propyne	6.87	71.0	8.08	103.0
1-butyne	6.80	78.8	7.52	100.8
1-pentyne	6.04	68.7	5.77	54.5
1-hexyne	4.90	46.4	7.17	119.0
1-octyne	4.51	42.3	7.63	147.3

Table 6. Nonlinear Regression Fit to Volumetric Growth Rate [μm^3 s^{-1}] of Alkynes vs Inv. Laser Power at Constant Pressure, $P_o = 2.0$ bar

precursor	ln($k_{v,P}$)	E_1 [W]	E_2 [W^2]
propyne	18.8	4.47	−0.76
1-butyne	18.5	5.18	−0.98
1-pentyne	16.7	3.83	−0.64
1-hexyne	17.0	5.04	−1.02
1-octyne	16.3	4.66	−0.94

Using linear regression, apparent activation energies were derived for each precursor with eq 2, and are listed in Tables 4 and 5 for the alkenes and alkynes, respectively. For the alkenes, E'_a averaged 34.2 kJ/mol-K at temperatures below 2000−2200 K; this is labeled region (I) in Figure 5A. Above 2000−2200 K, the average activation energy jumped to 60.2 kJ/mol K; this is labeled region (II). The average slope increased by a factor of 1.76 between these two regions. For the alkyne precursors, a change in E'_a was also apparent; within region (I), the average E'_a value was 61.43 kJ/mol K, while in region (II), the average E'_a was 104.9 kJ/mol K. In this case, the slope again increased by a factor of 1.70.

Volumetric Growth Rates. From eq 4B, the steady-state volumetric growth rate, k_v, can be approximated by:

$$k_v \cong \pi r_s^2 k_n \propto \frac{\chi_m}{\rho_d}\rho_g D_{12}\left[\nabla m_1 + \frac{m_{p,1}\cdot m_{p,2}}{\bar{m}_p^{\,2}}\alpha_T \nabla \ln(T)\right]\cdot\hat{n} \quad (15)$$

To relate this expression to the axial deposition rates of Figures 3 and 5, steady-state fiber radii were measured for each data point with an SEM; results for k_v are shown in Figure 6, A and B. It was found that the natural log of the volumetric growth rate followed the inverse laser power with a quadratic fit, $f(1/Q)$, at constant pressure, P_o. Defining the dimensionless laser power, $Q' = Q/Q_o$, where $Q_o \approx 1$ W, we have:

$$k_v = k_{v,P}[e^{-f(1/Q')}]|_{P=P_o} \quad (16)$$

or

$$k_v = k_{v,P}[e^{-(E_1[1/Q']+E_2[1/Q']^2)}]|_{P=P_o} \quad (17)$$

This equation is analogous to the standard activation energy equation, eq 2, with the dimensionless laser power as the independent variable rather than temperature.

By nonlinear regression, it was possible to derive "activation-energy-like" constants, E_1 and E_2, for the quadratic expression in eq 17; these are calculated for the alkynes in Table 6 as well as the volumetric rate constant at constant pressure,

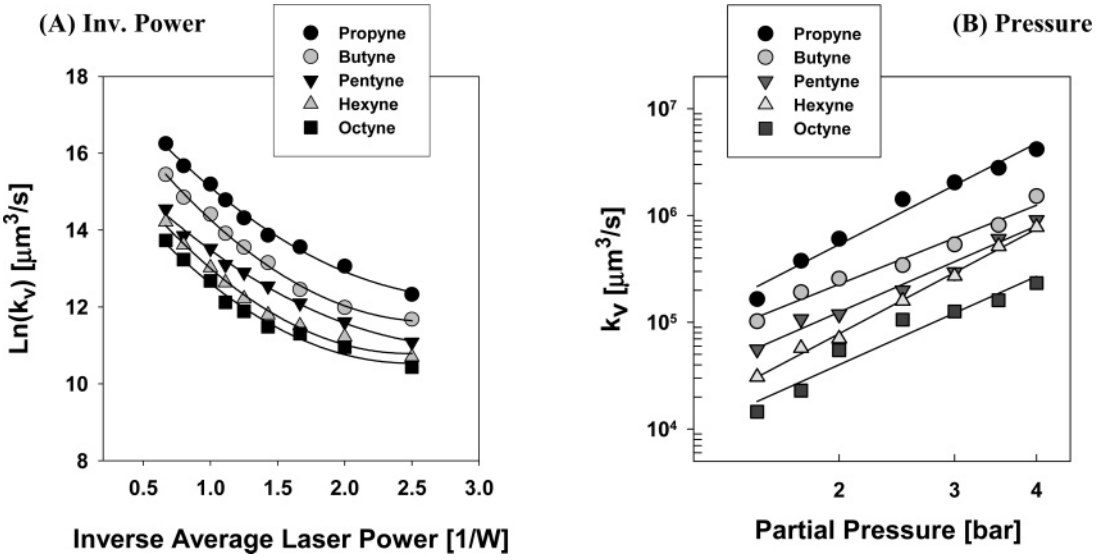

Figure 6. Volumetric growth rates for the alkynes vs. inverse laser power (A) and pressure (B). For (A), the pressure was held constant at 2.0 bar in all cases.

$k_{v,P}$—assuming a constant spot size and precursor partial pressure of 2.0 bar. Note that $k_{v,P}$ is also the extrapolated growth rate at infinite laser power. The series expansion of eq 17 about $Q' = 1$, gives:

$$\frac{k_v}{k_{v,P}} \approx \alpha + \beta\left[\frac{Q}{Q_o} - 1\right] + \frac{1}{2}\gamma\left[\frac{Q}{Q_o} - 1\right]^2 + \cdots \qquad (18)$$

where:

$$\alpha = e^{-(E_1+E_2)}$$

$$\beta = (E_1 + 2E_2)\, e^{-(E_1+E_2)}$$

and

$$\gamma = ((E_1 + 2E_2)^2 - 2(E_1 + 3E_2))\, e^{-(E_1+E_2)}$$

Through eqs 18 and 15, it is possible to measure transport parameters, such as χ_m, D_{12}, and α_t, using experimental data of fiber growth rates, diameters, deposit densities, laser powers, and measured temperature gradients. This approach also provides a tool for studying thermodiffusion in microchemical processes.

In addition to the Soret effect, temperature-induced bouyancy drives natural convection within the chamber. In the absence of externally imposed forced flow, convective plumes will rise from the tip of a heated fiber. Within a *small* chamber, a mixed forced convective cell can build within the enclosure, enhancing the free-stream gas velocity past the growth zone. This will lead to nonlinear increases in the growth rate with laser power, as seen in eq 18. Higher-order terms in eq 18 may also be due to the exothermic nature of the reactions; however, at 2.0 bar, the contribution of the heat of reaction remains 1−2 orders of magnitude less than the heat from the incident beam[10,20] which is insufficient to explain the features of Figure 6A. Further experiments will be needed to clarify the source of this nonlinearity.

Table 7. Linear Regression Fit to Volumetric Growth Rate [μm^3 s^{-1}] of the Alkynes vs Pressure [bar] at Constant Laser Power, Q_o = 550 mW

precursor	$\ln(k_{v,T})$	n_v
propyne	11.01	3.15
1-butyne	10.64	2.46
1-pentyne	9.88	2.68
1-hexyne	9.00	3.26
1-octyne	8.68	2.75

From the data in Figure 6B, the volumetric rate constant, $k_{v,T}$, and the volumetric reaction orders, n_v, were also determined for the alkynes using:

$$k_v = k_{v,T} \cdot P^{n_v}|_{T=T_o} \qquad (19)$$

Linear regression fits for these parameters are provided in Table 7; in each case, the laser power was held constant at 550 mW. The average volumetric reaction order for the alkynes was found to be 2.86—similar to the average *axial* reaction orders found previously of 3.07 and 3.29 in regions (A) and (B), respectively.

From eqs 17 and 19, together with the constants in Tables 6 and 7, it is possible to predict the volumetric growth rate for the alkynes over a wide range of laser powers and pressures, provided laser spot sizes and chamber dimensions are employed that are similar to those in this work.

V. Discussion

An important structural difference between the 1-alkenes and the 1-alkynes is the angle of the bond joining the multiply bonded C-atoms and the hydrocarbon tail. In the alkenes, the tail lies at approximately 120° relative to the doubly bonded carbon atoms, while in the case of the alkynes, the tail is forced to lie in the direction of the triple bond,[21] i.e. for the alkenes (I) and alkynes (II), respectively:

(20) Maxwell, J. L. *Three-dimensional Laser-induced Pyrolysis: Modeling, Growth Rate Control, and Application to Microscale Prototyping.* Ph.D. Thesis, Rensselaer Polytechnic Institute 1996, pp131−132.

(21) Mollere, P. D.; Houk, K. N.; Bomse, D. S.; Morton, T. H. *J. Am. Chem. Soc.* **1976**, *98* (16), 4732−4736.

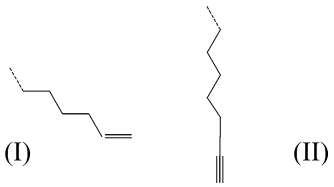

Provided the terminal double- or triple-bonds are responsible for adsorption, it becomes increasingly difficult for the alkynes to adsorb as χ increases—due to steric resistance. For the alkynes, adsorption likely occurs through π-bonds of the triple bond—with the alkyne tail oriented normal to the deposit surface. In contrast, the 120° angle of the alkene chains leaves a more open geometry for adsorption of the terminal carbons—and the chains can adsorb in many configurations; in this case, χ does not greatly influence the adsorption rate, and the hydrocarbon tail lies adjacent to the surface, increasing the probability that tailing carbon atoms will also be deposited.

It is also known that the terminal double and triple bonds of the 1-alkene and 1-alkyne molecules are strong compared to other C−C bonds in each chain—and that the double bond of the alkenes is more reactive that that of the alkynes.[22] In addition, bonds immediately adjacent to the double and triple bonds, i.e. the allylic and propargyl bonds, are the weakest in each chain. It is also known that the double bond in the alkene chains is relatively mobile—and with additional energy can move to alternate locations along the chain. In contrast, the triple bond of the alkynes is relatively immobile; it requires the relocation of two hydrogen atoms to swap the triple bond to an adjacent location. This creates a situation where the 1-alkenes can be readily transformed—and subsequently dissociate into smaller intermediates, while the alkynes are more rigid—and more likely to transport intact and then decompose at the propargyl bond.

One potential explanation for the inverse m_p dependence of the alkynes (refer to Table 1, eqs 8, 14A, and 14B) is that a large portion of each alkyne chain is lost and returns to the gas phase through the normal surface adsorption orientation and reduced propargyl bond strengths. In this scenario, χ_d drops with molecular weight both through limited adsorption from steric effects and desorption of large portions of the hydrocarbon chain.

An alternative explanation for the inverse m_p effect is that low m_p reaction byproducts, such as atomic hydrogen and H_2 build up near the fiber surface due to the Soret effect. Provided the alkyne molecules remain intact during transport, the mass difference between reactants and byproducts is large, and thermal diffusion is strong. In contrast, the alkenes may dissociate in the gas phase, such that the mass differential is less pronounced. The $(m_{p,1}\cdot m_{p,2}/\bar{m}_p^2)\cdot\alpha_t$ coefficient of the thermodiffusion term in eq 4B tracks closely the inverse relationship found in Table 1 ($\chi_{d,a}$); in this case, excess H or H_2 at/near the surface will inhibit the reaction by displacing the alkynes—and the rate-limiting step in region A of Figures 3 and 4B will be the desorption/transport of hydrogen from the reaction zone.

Divergent reaction orders for the alkynes in region B (see Table 3 and Figure 4B) are consistent with both the low-carbon yield per molecule and the Soret effect. However, the Soret effect alone cannot fully explain the more extreme m_p-dependence in region B (see Table 1, $\chi_{d,b}$). If $\chi_d \ll 1$, growth rates will diverge due to the inverse m_p-dependence in eqs 5 and 6, provided most molecules remain intact prior to arriving at the surface; these differences will be exaggerated as the mean free path decreases. If, on the other hand, a set of common intermediates are formed (as may readily occur for the *alkenes*—see Figure 3, region B), growth rates will tend to converge as the pressure rises and increased homogeneous reactions occur.

In evaluating the cause of the reaction-order transition between regions (A) and (B) in Figure 3, observe that the transition is absent for the volumetric growth rates in Figure 6B. Regardless of changes in the axial reaction order, the fiber diameter compensates, and the overall *volumetric* reaction order remains unchanged; n_v also does not vary greatly with molecular weight (see Table 7). Thus, the cause of the region (A) → (B) transition cannot be a long-range transport phenomenon—rather a local effect of carbon yield and/or thermodiffusion.

Regarding activation energies, the similarity of the slope transition between regions (I) and (II) in Figure 5—regardless of the structure of the precursor—supports a morphological change in the deposit as a root cause, rather than transport effects. This transition likely corresponds to a previously observed phase change from parabolic graphite to nodular

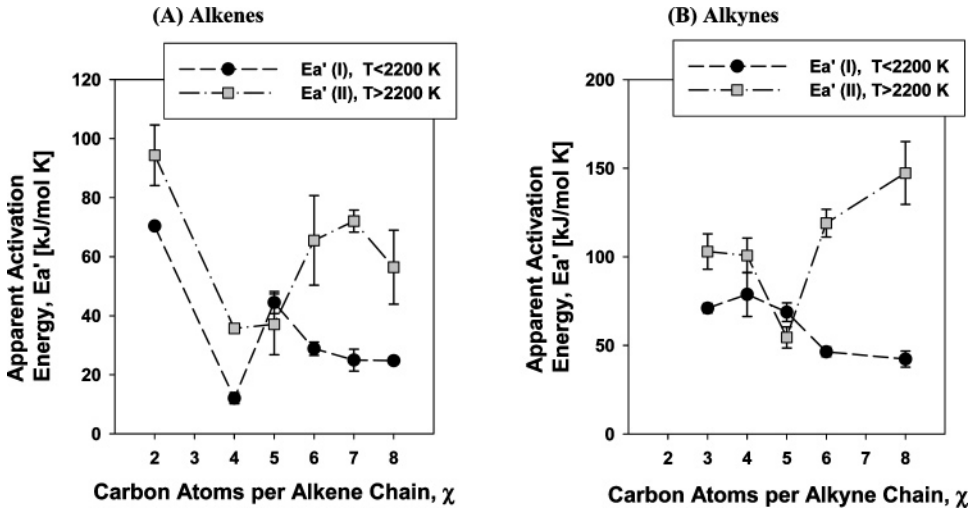

Figure 7. Apparent activation energies for the alkenes (A) and alkynes (B) vs. precursor molecular weight for regions E_a' (I) and E_a' (II). Error bars correspond to the standard error. Pressure held constant at 2.0 bar in all cases.

graphite at approximately 2200 K.[10] Note, however, that pentene and pentyne follow slopes intermediate to both regions (I) and (II); this can be clearly seen in Figure 7, where apparent activation energies are plotted for each region vs m_p—including error bars that correspond to the standard error. For pentene, data fall within the standard error for both regions—implying that little or no temperature dependence in E_a' ccurs for pentene over the entire temperature range. Similarities between pentene and pentyne E_a' values suggest related transport and growth mechanisms.

Finally, note that the difference in E_a' between regions (I) and (II) of Figure 7 is most pronounced for chains with more than six carbon atoms. In addition to the phase change described earlier, a change in reactant transport may also occur at high temperatures where $\chi \geq 6$. This may be due to the formation of atomic hydrogen at temperatures in excess of 2000−2200 K, which would further enhance the Soret effect. Further mechanistic and spectroscopic studies will be needed to determine precise reaction pathways for both the alkenes and alkynes, taking into account the formation of intermediates and the potential for polymerization and cyclization in the gas phase.

VI. Conclusions

Several important phenomena were observed in this study. First, the axial growth rate of the alkenes is approximately proportional to the square root of the molecular mass of the precursor, while for the alkynes an inverse relationship holds. The m_p-dependence of the alkynes is attributed to greater steric resistance of adsorption/reaction than the alkenes and/or the Soret effect. Second, the reaction order for the alkenes is approximately 1.65, while for the alkynes, two regions are observed with average $n = 3.07$ and 3.29. Third, both the alkenes and alkynes exhibit two regions of activation energy—and it is suggested that the transition is caused primarily by a phase change in the deposit material. The notable exceptions to this rule are the aliphatic chains with five carbon atoms, i.e., pentene and pentyne. In addition to the aliphatic molecules, a cyclic hydrocarbon, benzene was tested—and it exhibited the greatest axial growth rates of all—exceeding 10 mm s^{-1}.

Finally, a complete set of empirical growth rate equations are available for carbon fiber growth from the alkenes and alkynes; using eqs 7, 8, 12A, and 12B and substituting data for n and E_a' from Tables 2−5 into eq 2 gives expressions for each precursor in the transport-limited regime. Volumetric rate parameters were also derived for the alkynes, and it was shown that k_v increases nonlinearly with laser power—mostly likely due to convective flow within the chamber.

Acknowledgment. We gratefully acknowledge the Los Alamos National Laboratory LDRD-ER program for funding this work. Our thanks also go to H. Grennberg, K. Maskaly, J. Boncella, T. Cremers, and M. Black for useful discussions.

JA057666J

(22) Choudary, N. V.; Kumar, P.; Bhat, T. S. G.; Cho, S. H.; Han, S. S.; Kim, J. N. *Ind. Eng. Chem. Res.* **2002**, *41* (11), 2728−2734.